Supporting Information

Highly Selective Electrocatalytic Oxidation of Amines to Nitriles Assisted by Water Oxidation on Metal Doped α-$Ni(OH)_2$

Yuxia Sun,[a,‡] Hyeyoung Shin,[b,‡] Fangyuan Wang,[a,‡] Bailin Tian,[a] Chen-Wei Chiang,[a] Shengtang Liu,[a] Xiaoshan Li,[a] Yiqi Wang,[a] Lingyu Tang,[a] William A. Goddard III,[c]* and Mengning Ding [a]*

[a]Key Laboratory of Mesoscopic Chemistry, State Key Laboratory of Analytical Chemistry for Life Sciences, School of Chemistry and Chemical Engineering, Nanjing University, Nanjing 210023, China

[b]Graduate School of Energy Science and Technology (GEST), Chungnam National University, Daejeon 34134, Republic of Korea

[c]Materials and Process Simulation Center (MSC) and Liquid Sunlight Alliance (LiSA), California Institute of Technology, Pasadena, California 91125, United States

Table of Contents

1. Experimental Procedures

1.1 Preparation of anodic materials

Firstly, for the preparation of Mn doped α-$Ni(OH)_2$/Ni foam, the nickel foam (NF, 1x2 cm, 1 mm thick) was pretreated in sequence under ultrasonication with acetone, 3.0 M HCl(aq), ethanol and deionized water for 15 min. After drying under vacuum, the Mn doped α-$Ni(OH)_2$/Ni foam was synthesized via a hydrothermal process. In a typical synthesis, 1.275 mmol nickel nitrate hexahydrate, 0.225 mmol Mn(II) nitrate, and 3.75 mmol urea were dissolved into 15 mL of deionized water. Then the solution was transferred to a 20 ml Teflon-lined autoclave and two pieces of pretreated Ni foam were immersed into it. Afterwards, the autoclave was heated at 100 ^oC for 3 h. The obtained Mn-doped α-$Ni(OH)_2$/Ni foams were washed with ethanol and deionized water several times, and then dried under vacuum at 60 ^oC overnight. For synthesis of other metal doped α-$Ni(OH)_2$/Ni foams, the corresponding metal salts were adopted as substitution for manganese nitrate, respectively.

1.2 General Characterization

XRD patterns were collected on a Shimadzu Lab X/XRD-6000 X-ray diffractometer equipped with a Cu-Kα radiation source (λ= 0.15418 nm) operating at 40 kV and 30 mA. SEM image were recorded on Hitachi S-4800 with samples deposited on carbon conductive tapes. TEM and High-resolution TEM images were obtained on JEOL JEM-1011 and JEM-2100 with samples deposited on carbon coated Cu grids, respectively. Raman spectrum was recorded on a Horib France Sas Xplora Plus Raman spectroscope equipped with a 532 nm laser source. X-ray photoelectron spectroscopy (XPS) was performed on a UlVAC-PHI 5000 Versa Probe spectrometer with Al Kα as radiation source. The binding energies were calibrated by the C 1s peak, the internal standard reference at 284.6 eV.

1.3 Electrochemical methods

Electrochemical experiments were carried out in an undivided electrochemical cell with a standard three-electrode system using a Corrtest CS3004 electrochemical workstation. Platinum foil and the prepared anodic materials were used as the counter and working electrode, respectively. An Hg/HgO electrode (1 M KOH, pH=13.5) was used as the reference electrode and the potentials were calibrated by RHE (E (vs RHE) =E (vs Hg/HgO) + 0.059*pH). To exclude the effect of Nickel foam on the tafel slope of anodic oxidation, cyclic voltammetry (CV) curves were recorded using glass carbon electrode (3mm diameter) as the working electrode. The ink was prepared by dispersing 5 mg catalysts in a mixture of 960 μL isopropanol and 40 μL Nafion solution (5 wt%, DuPont) via sonication. 5 ul ink was dropped on the bare glass carbon electrode (GCE) and dried under infrared lamp for use. 1 M KOH aqueous solution was used as the electrolyte, with the total volume to be 20 mL. All the potentials were not IR compensated. For each bulk electrolysis measurement, 20 mL of electrolyte containing a specified amount of benzylamine was added into the undivided cell with a micro-magnetic spin bar for stirring. After the reaction finished, the whole reactant was extracted with ethyl acetate instantly. After the internal standard dodecane added, the organic phased was sampled for GC analysis. For the examination of OH^- dependence of catalytic current at Mn doped α-$Ni(OH)_2$/NF by varying the concentration of OH^-, K_2SO_4 was added as the supplement to maintain the approximate ionic strength. To obtain electro-kinetic data in Figure 3f, the chronoamperometry analysis was conducted at 1.4 V (vs RHE) until the charge was passed for 4-30 C dependent on the substrate concentration. The nitrile partial current was calculated by the (I_{total}*Faradic efficiency of Nitrile). (I_{total}, the average current is calculated to be the charge divided by time).

To elucidate the rationality of undivided cell, a set of control experiments were carried out. First, to exclude the possible effect of cathode to the anodic product in the undivided cell, a divided cell setup was adopted. The cathodic LSV scan was conducted with and without benzyl nitrile added in the cathode side. The current with benzyl nitrile showed a negligible decrease, demonstrating that the nitrile product was not significantly reduced on the cathode, which is probably not thermodynamically preferred compared to HER. Secondly, in a divided cell with proton exchange membrane, benzyl amine was placed in the anodic cell with other conditions remained. GC analysis showed no obvious change in the corresponding nitrile yield compared to that of undivided cell. That is, the use of undivided cell will not cause side reactions in the system, making the setup of undivided cell reasonable. The Ar gas flow rate was set as 20 mL min^{-1} during the cathodic HER measurement to maintain a constant system. The gas products were continuously analyzed by on-line gas chromatography (GC-9860-5C-NJ) equipped with a thermal conductivity detector (TCD) and two flame ionization detectors (FID).

1.4 In situ measurement procedures

In situ electrochemical impedance spectroscopy (EIS) tests were measured using a CHI660E electrochemical workstation over a frequency range from 10^4 to 10^{-1} Hz with AC amplitude of 5 mV.

In situ Raman spectroscopy In situ Raman measurement is performed using XPlora PLUS (Horiba Scientific), and the excitation wavelength of the laser is 532 nm.

In situ conductivity measurement: Fabrication of the NiMn catalysts devices. The free standing films were prepared by a co-solvent evaporation method.[1] A PMMA film was prepared by spin coating on the substrate (p++ silicon wafer with 300 nm thermal oxide) surface with pre-patterned Ti/Au electrodes (20/50 nm). The NiMn catalysts films were then transferred onto the substrate surface. After the removal of PMMA template, NiMn catalysts films were deposited on the device with desired patterns. Another layer of PMMA (electrochemically inert) was then deposited on the device with NiMn catalysts film patterns and a smaller window that only exposes catalysts was opened by e-beam lithography. The final device, with exposed NiMn catalysts was used for on-chip electrochemistry and *in situ* electrical transport spectroscopy (ETS) measurements, which were performed by a 2-channel source measure unit (Keysight B2902A). The *in situ* electrical conductivity was calculated by:

$$\sigma = \frac{I_{\mathrm{cond}} \times l}{V_{\mathrm{DS}} \times w \times h \times N}$$

where I_{cond} is the conductive current, l is the length of electrochemical window, w is the width of electrochemical window, V_{DS} is the small bias voltage (50 mV) between drain and source electrodes, h is the average film thickness determined by AFM, N is the number of devices connected in parallel.

1.5 Product analysis

Three independent electrolysis experiments were conducted with each catalyst for performance evaluation. Gas chromatography measurements were conducted on Shimadzu Nexis GC-2030 with a flame ionization detector and SH-Rtx-1 capillary column (30 m, 0.25 mm ID, 0.25 μm df). For quantitative analysis, the sample was injected for 3 times to get a mean value for one electrolysis. The temperature of the column was initially kept at 70 °C for 1 min and first increased to 150 °C at a rate of 10 °C/min. Then the temperature was increased to 250 °C at a rate of 25 °C/min and kept for 3 min. Dodecane was used as the internal standard to quantify the substrate and products. The quantification of H_2 was carried out by Gas chromatography (GC-9860-5C-NJ) with a thermal conductivity detector (bridge current set as 75 mA) and two flame ionization detectors (FID). The conversion of benzyl amine and the yields of benzyl nitrile were calculated as follows.

Conversion= (1- moles of amine /moles of amine loaded) ×100%

Yield= (moles of product/moles of amine loaded) ×100%

$FE_{nitrile}$(%) = mol of nitrile/[total passed charge/(4 × F)]×100%

FE_{H2}(%) = mol of hydrogen/[total passed charge/(2 × F)]×100%”

1.6 Computational details

Spin-polarized density functional theory calculations were carried out using the Vienna Ab-initio Simulation Package (VASP) code.[1] Perdew−Burke−Ernzerhof (PBE) exchange-correlation functional[2-3] along with the D2 atom pairwise dispersion corrections[4] was employed and the core-valence interaction was described by the projector augmented wave method.[5] The plane-wave cutoff energy was set at 400 eV and the dipole correction was applied in the direction perpendicular to the surface. To calculate how the free energies depend on the applied potential (vs. RHE) at room temperature (298.15 K) and pH=13.5, the grand canonical quantum mechanics calculations were performed with the charge-asymmetric nonlocally determined local-electric (CANDLE) implicit solvation model[6] and the GBRV ultrasoft pseudopotentials[7] using the joint density functional theory (JDFTx).[8] All other settings for JDFTx calculations are similar to those for VASP calculations. The zero-point energy, enthalpy and entropy contributions to the free energy of each state were computed from the molecular vibrational terms using VASP as in our previous studies.[9-10] In this work, the NiOOH electrocatalyst was modeled using the gamma-phase crystal structure of NiOOH suggested by Ceder group.[11] After bulk crystal optimization process, a (100) slab model of NiOOH with one explicit water monolayer was constructed, and it was confirmed that the interplanar spacing, oxygen stacking and average oxidation state of nickel elements in this model were in good agreement with experiments as we discussed in the previous work.[12-13] For (Mn,Ni)OOH, we first identified the most stable Mn doping site on the pristine surface of gamma-phase NiOOH (100) and found the most stable equilibrium surface structure under the experimental electrochemical operating conditions by considering the surface free energy diagram as shown in Figure S22. Both the NiOOH and (Mn,Ni)OOH surface models used in the mechanistic studies are represented in Figure S21. Each surface model consists of four layers and vacuum area of 15 Å. For optimization of the surface models, the two layers at the top were relaxed while the other two layers at the bottom were fixed. In addition, all possible oxidation steps and configurations were examined to clarify the reaction pathways with the lowest free energy for both amine and water oxidation.

2. Results and Discussion

2.1 The SEM, TEM images, XRD patterns, and XPS spectra of the prepared catalysts.

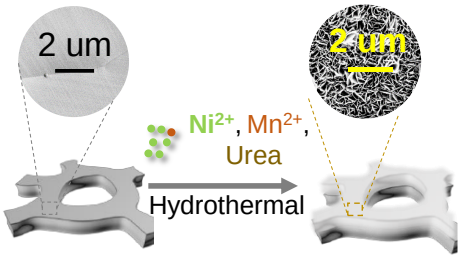

Figure S1. Synthetic scheme of the prepared catalysts.

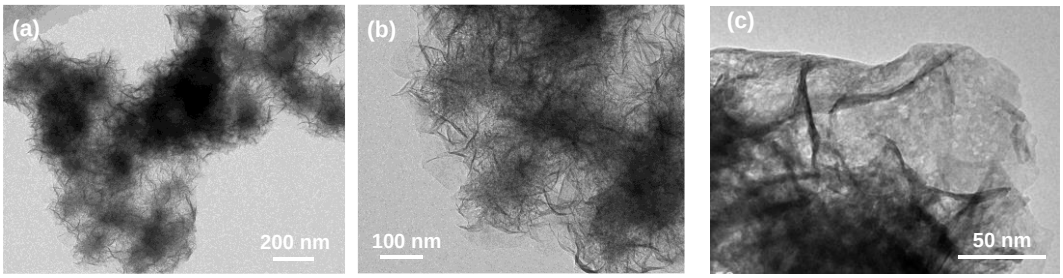

Figure S2. (a -c) TEM images of the prepared Mn doped α-$Ni(OH)_2$.

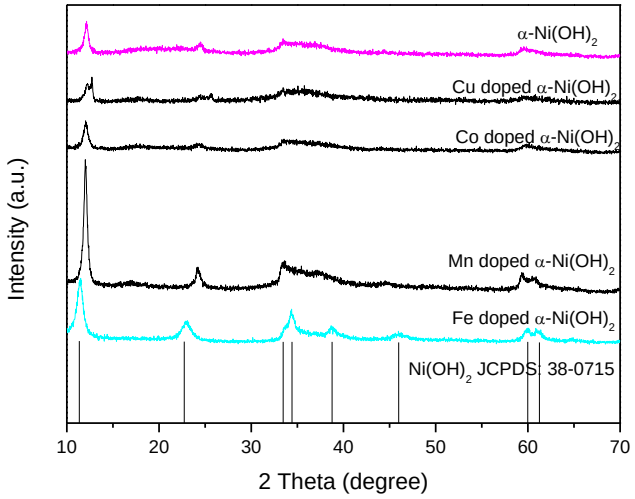

Figure S3. XRD patterns of the as-prepared pristine and metal-doped α-$Ni(OH)_2$ catalysts.

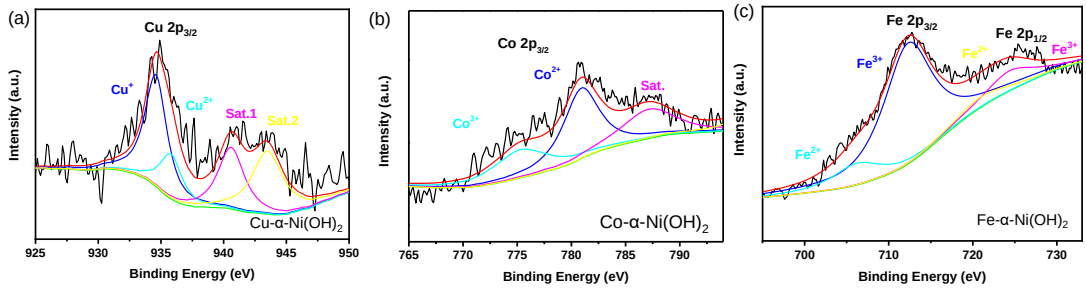

Figure S4. The 2p XPS spectra of metal doped α-Ni $(OH)_2$.

For the high-resolution Co 2p2/3 XPS spectrum, binding peaks of 2p2/3 at approximately 778.4, 781.6 eV and 787.2 eV are assigned to Co^{3+}, Co^{2+} and satellite respectively.[14] This demonstrated the presence of Co^{3+} and Co^{2+} in the doped material.

For the Fe 2p XPS spectrum, peaks centered at binding energy of 707.0 and 722.2 eV were observed, assigned to Fe2+ 2p3/2 and Fe2+ 2p1/2, respectively; peaks at 712.1 and 725.8 eV can be attributed to Fe^{3+}2p3/2 and Fe^{3+}2p1/2, respectively. [15]

For the Cu 2p XPS spectrum, the Cu 2p spectra can be deconvoluted into peaks: Cu^{+}(932 eV), Cu^{2+}(934 eV), and satellite peaks (941 and 943 eV). [16]

2.2 The electrochemical data of the prepared Mn doped α-Ni(OH)$_2$ for BA oxidation

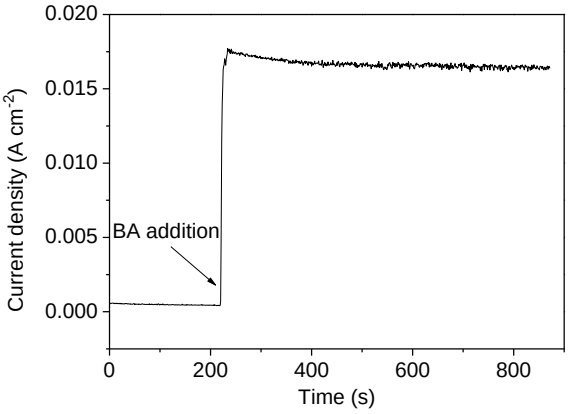

Figure S5. The anodic current on Mn doped α-Ni $(OH)_2$/Ni foam in 1 M KOH system upon BA addition.

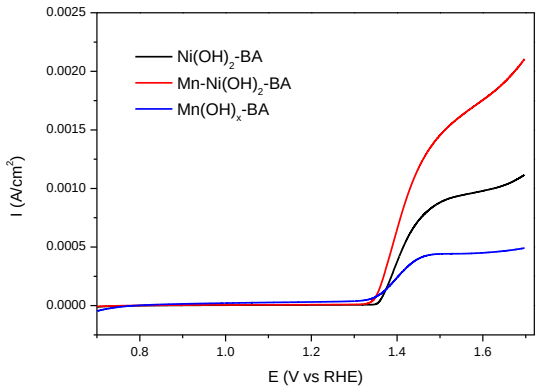

Figure S6. The LSV plots of the prepared catalysts on GC electrode for BA oxidation.

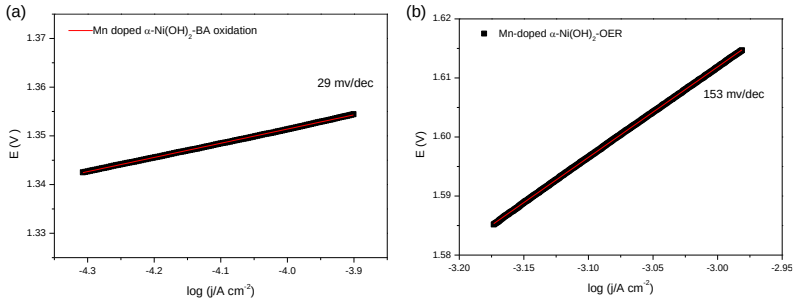

Figure S7. The tafel data of the prepared Mn doped α-Ni(OH)$_2$ for BA oxidation and OER. Note that to exclude the interference of Ni foam, catalysts on glass carbon (GC) were adopted as the anode to obtain the corresponding Tafel, which resulted in relatively small current densities.

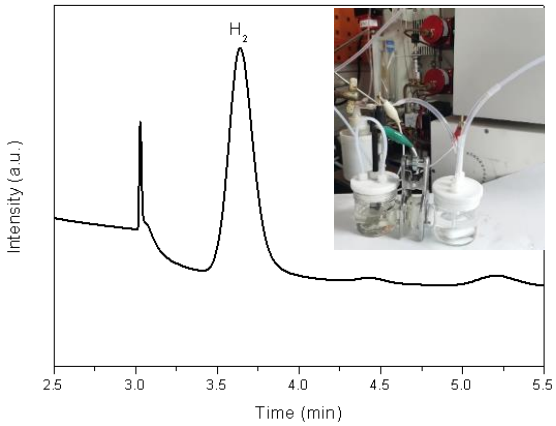

Figure S8. The typical GC plot of the H_2 for cathodic HER

The Ar gas flow rate was set as 20 mL min^{-1} during the cathodic HER measurement to maintain a constant system. The gas products were continuously analyzed by on-line gas chromatography (GC-9860-5C-NJ) equipped with a thermal conductivity detector (TCD) and two flame ionization detectors (FID). The faradic efficiency for HER was about 97.8%.

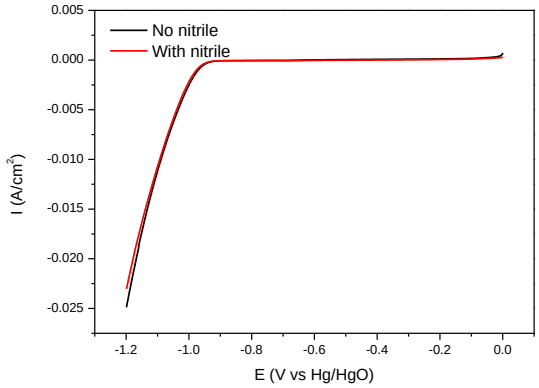

Figure S9. The LSV scan for cathodic HER with and without nitrile. The current with benzyl nitrile showed a negligible change, demonstrating that the nitrile product was not significantly reduced on the cathode.

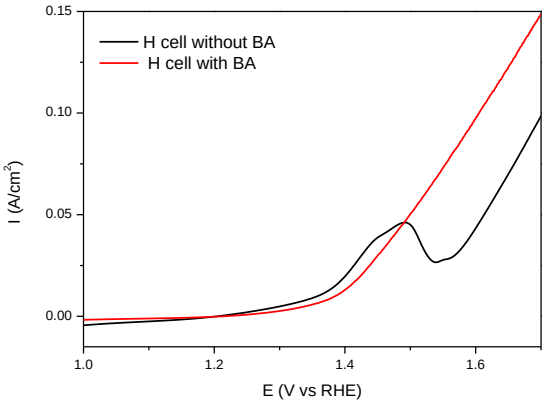

Figure S10. The LSV plot of the anodic oxidation with a H cell setup. A H-cell setup was adopted and the nitrile product was obtained with a 95.7% yield, close to that from the undivided cell. This illustrated the rationality of the setup and exclude HER effect on nitrile yield in this work.

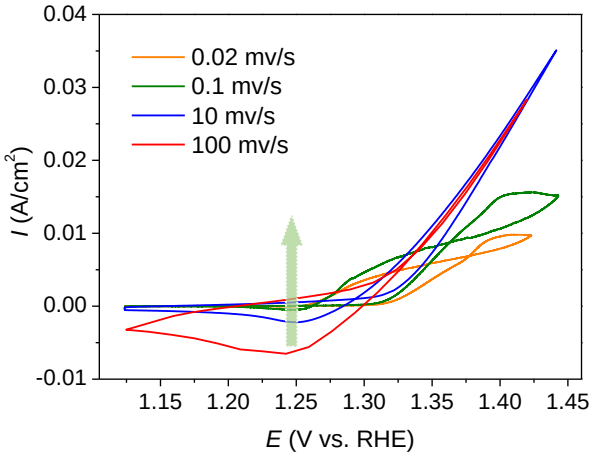

Figure S11. CV plots of Mn-Ni$(OH)_2$/Ni foam at varied scan rates.

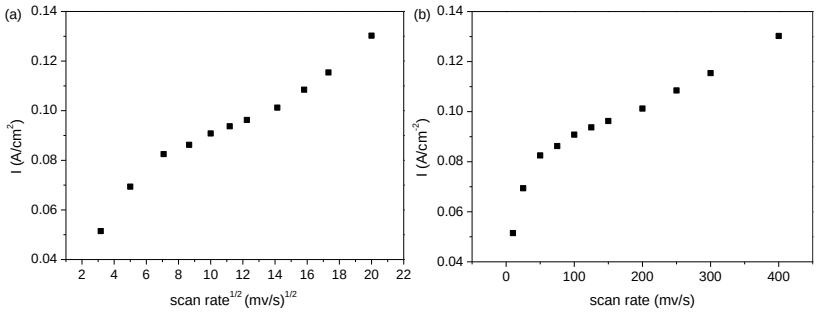

Figure S12. The relationship between the anodic peak current density and (a) the square root of scan rate or (b) the scan rate (v).

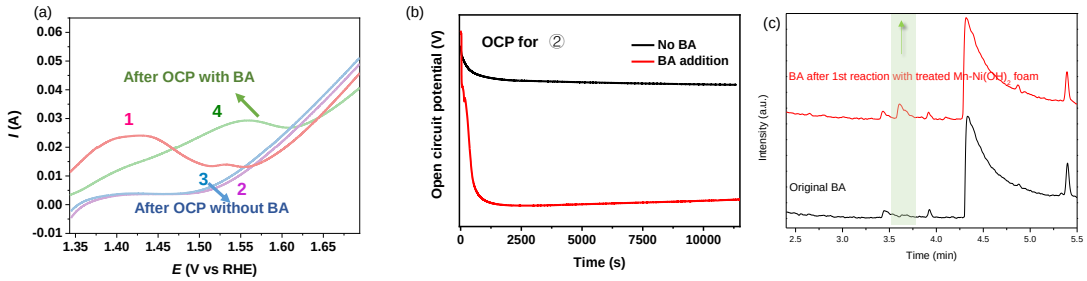

Figure S13. (a) LSV plots for the formed foams 1-4. (b) The open circuit for formed foam 2 recorded under different conditions. (c) The GC results of original BA and BA after reaction with the foam 2. The possible reaction of active species on the treated foam with BA to form trace nitrile, as detected by Gas Chromatography analysis (c).

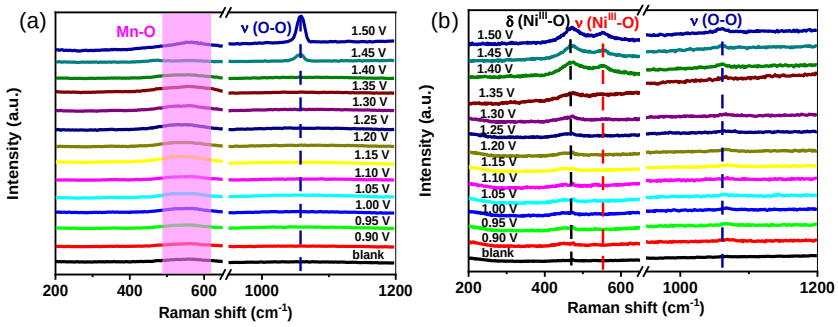

Figure S14. (a) In situ Raman spectra at various potentials (such as 0.9 to 1.5 V with 0.05 V intervals) of Mn doped α-Ni(OH)$_2$ (b) and α-Ni(OH)$_2$.

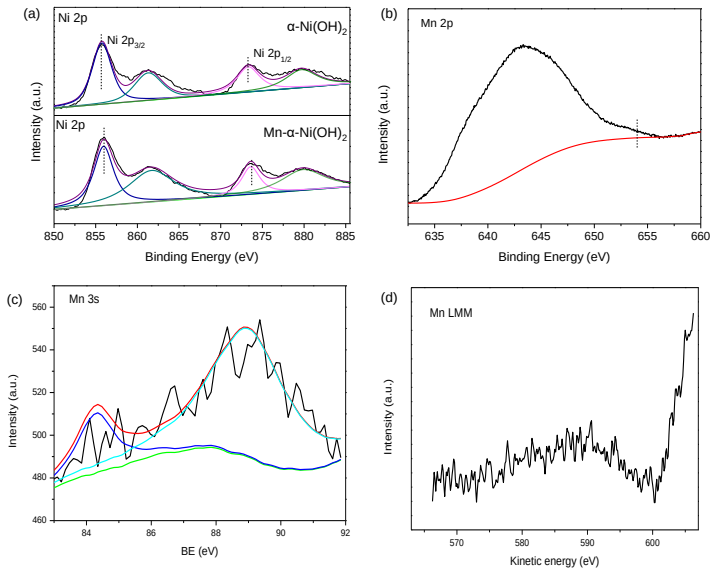

Figure S15. (a) Ni 2p XPS spectra of α-Ni $(OH)_2$ and Mn doped α-Ni $(OH)_2$/NF. (b) Mn 2p XPS spectra of Mn doped α-Ni $(OH)_2$. (c) The Mn 3s spectra (d) The Mn LMM auger spectra of the prepared Mn doped α-Ni$(OH)_2$. The Mn LMM auger signal was too weak to distinguish different states of the doped Mn. Instead, Mn 3s XPS was recorded.

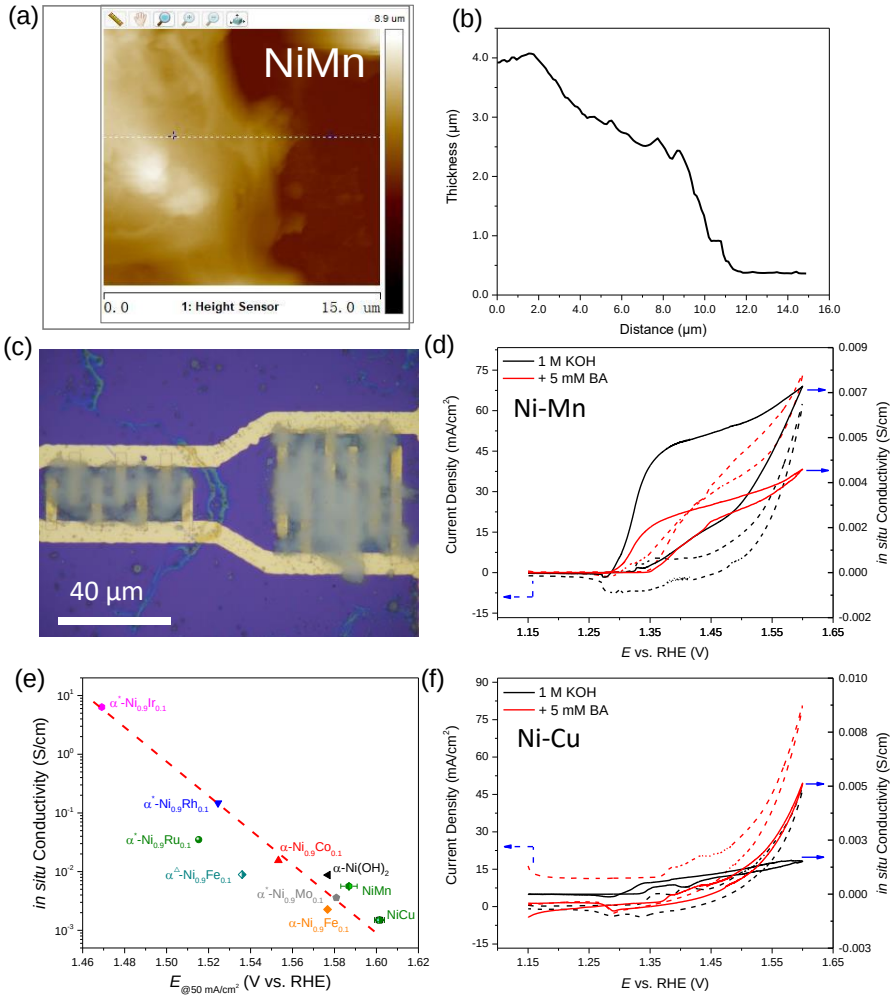

Figure S16. The on-chip electrochemical and in situ ETS measurements (a) Atomic Force Microscopy (AFM) image (b) height measurement of NiMn films on chip (c) Experimental setup of the fabricated chip. (d) cyclic voltammetry (CV) and electrical transport spectroscopy (ETS) curves of Mn doped $Ni(OH)_2$.(e) Summary of in situ conductivity and OER activity of metal doped Ni based materials. f) cyclic voltammetry (CV) and electrical transport spectroscopy (ETS) curves of Cu doped $Ni(OH)_2$.

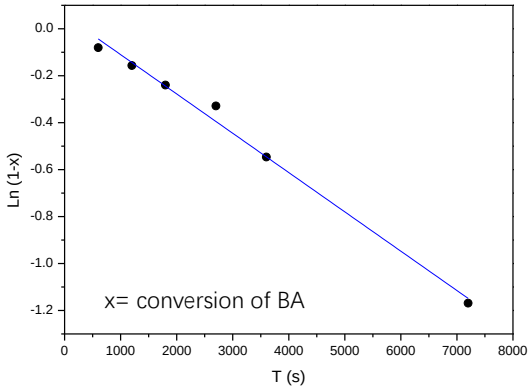

Figure S17. The plot of ln(1-x) versus reaction time. The plot of ln (1-x) vesus time (x= conversion of BA) present a linear relationship, further verifying the reaction order was close to one with respect to BA.

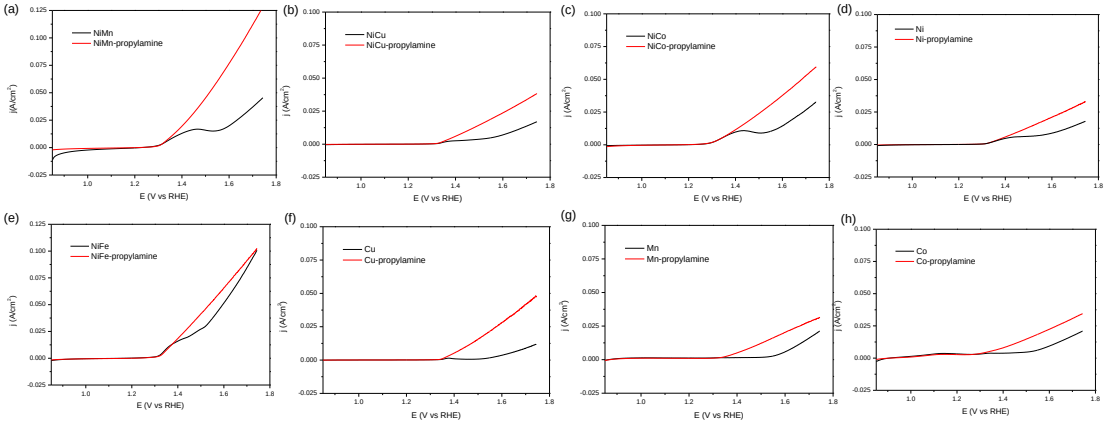

Figure S18. The LSV plots of propylamine oxidation on metal doped α-Ni $(OH)_2$ and metal hydroxides.

Considering the volatility of ethyl amine, the LSV test of propyl amine was conducted to verify the similarity of activities between R-CH_2-NH_2 structure and benzyl amine. A similar superior performance (96.9% yield of propyl nitrile, FE 97.0%) was obtained when further electrolysis of propyl amine by Mn doped α-Ni $(OH)_2$ was carried out under identical conditions of benzylamine. These results made it relatively reasonable for theoretical calculation with ethyl amine as the model substrate.

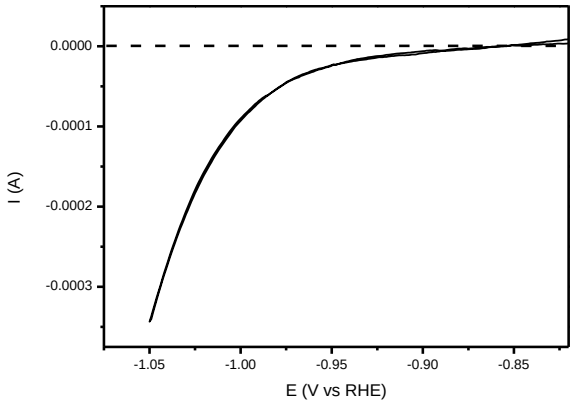

Figure S19. Single cycle CV curve of Hg/HgO electrode calibration in 1 M KOH. The calibration was conducted based on the experiment in a three-electrode system reported in literature (ACS Energy Lett. 2020, 5, 1083−1087): Pt foil (Aldrich) was selected as both the working electrode (WE) and counter electrode (CE). The electrolyte was saturated with high-purity hydrogen for 30 min. The CV was carried out at a scan rate of 1 mV/s, and the average of the two interconversion point values was taken as the thermodynamic potential.

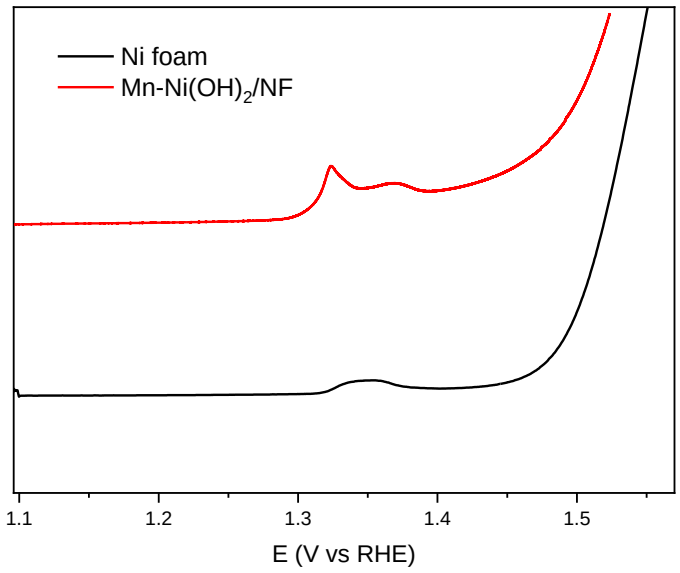

Figure S20. LSV curves of Ni foam and Mn-Ni$(OH)_2$/NF.

2.3 The DFT-calculated diagrams

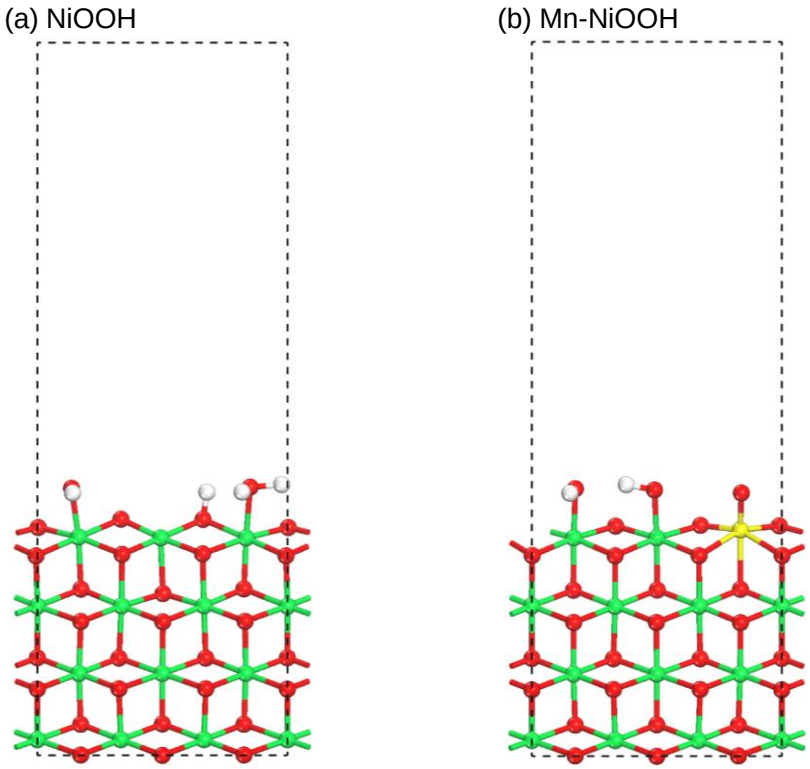

Figure S21. Computational models used for (a) NiOOH and (b) Mn-NiOOH (100) surfaces. For clarity the intercalating species such as K^+ and H_2O are not shown. Green, yellow, red and white spheres indicate Ni, Mn, O, and H atoms, respectively.

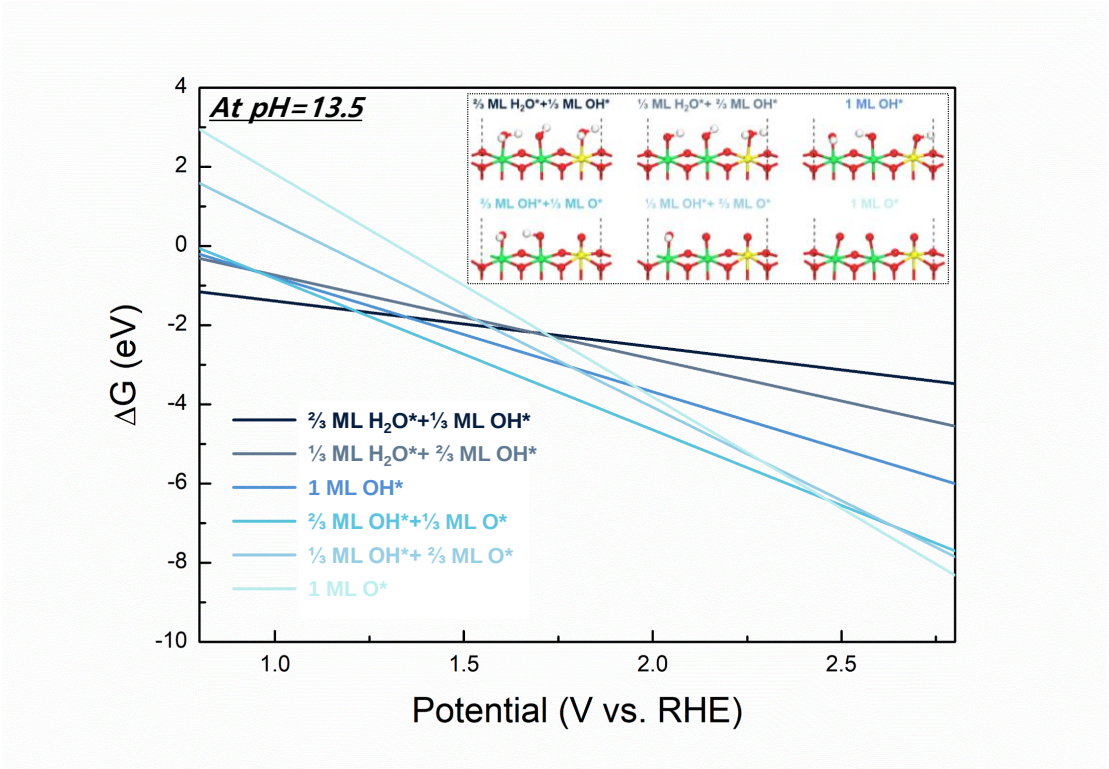

Figure S22. Surface free energy diagram of Mn-doped NiOOH (100) with different monolayer (ML) coverages of H_2O, OH, and O as a function of the applied potential (V vs RHE). Inset shows the DFT-calculated atomic configurations of each surface. Note that * denote an adsorbed state. For clarity the intercalating species such as K^+ and H_2O are not shown in the insets. Green, yellow, red and white spheres indicate Ni, Mn, O, and H atoms respectively.

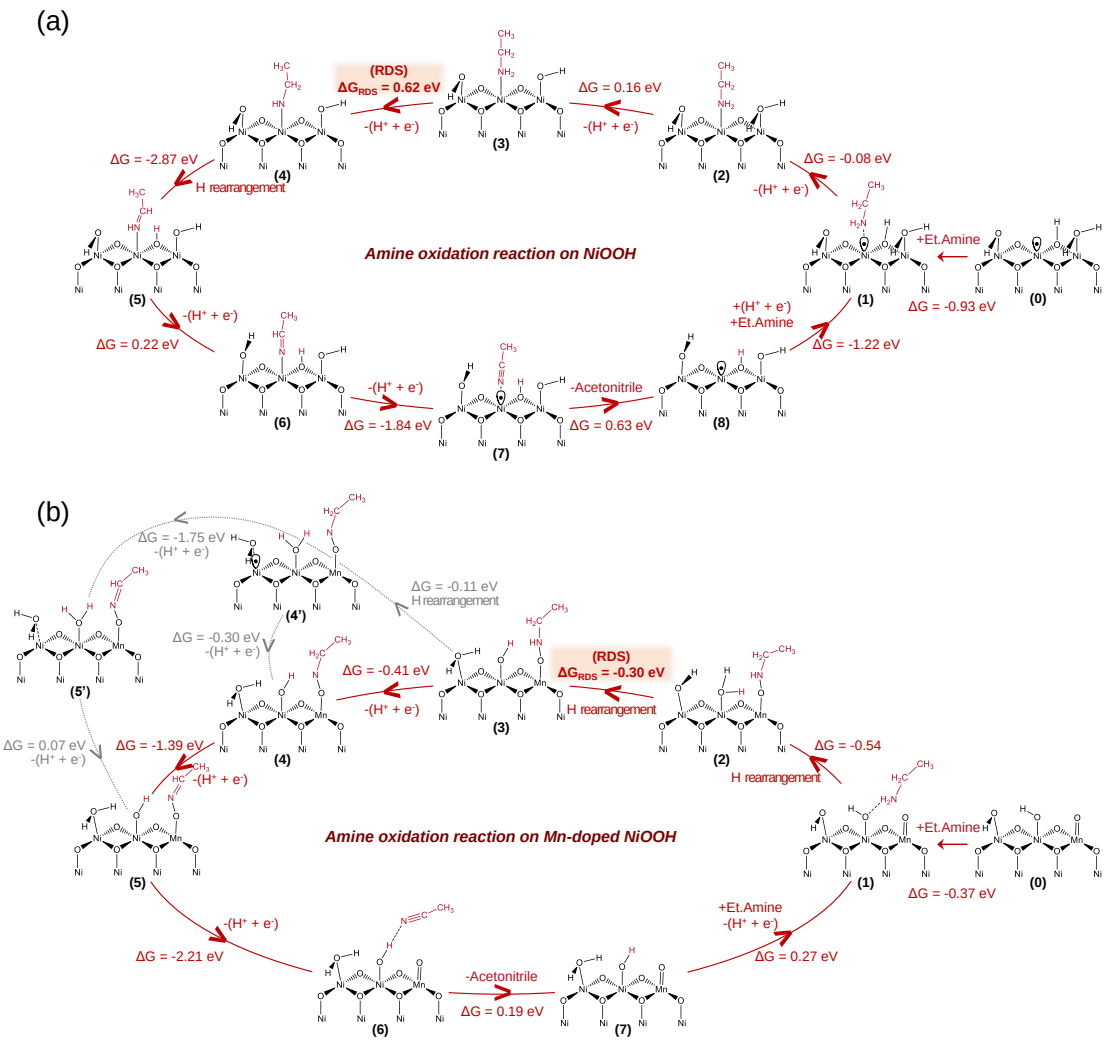

Figure S23. Full reaction free energy diagrams for the amine oxidation reaction on (a) NiOOH and (b) Mn-doped NiOOH (100) surfaces.

Table S1 The elemental doping ratio determined from ICP-OES data

ICP	n % M/(M+Ni)
Mn-α-$Ni(OH)_2$	3.3
Fe-α-$Ni(OH)_2$	25
Fe-α-$Ni(OH)_2$-2	11.8
Fe-α-$Ni(OH)_2$-3	4.1
Cu-α-$Ni(OH)_2$	1.78
Co-α-$Ni(OH)_2$	14.6

Table S2 The results of constant potential electrolysis under different potentials

Potential	Time	Charge	Conversion (%)	Yield (%)
Open potential	12	--	3.4	Not det
0.9	12	0.01412	7.1	Not det.
1.0	12	0.2416	8.9	Not det.
1.25	12	1.1073	6.2	Not det.

Table S3 The EIS fitting data of the metal doped Ni(OH)2 in 1 M KOH

Catalyst	Potential	R_s	R_{ct}
Mn-α-$Ni(OH)_2$	1.2	3.23	17.37
Mn-α-$Ni(OH)_2$	1.3	3.36	16.76
Mn-α-$Ni(OH)_2$	1.4	3.79	12.66
Mn-α-$Ni(OH)_2$	1.5	4.01	12.37
Mn-α-$Ni(OH)_2$	1.6	3.95	11.84
α-$Ni(OH)_2$	1.6	7.16	23.43
α-$Ni(OH)_2$	1.7	7.01	12.55

Table S4 The comparation of the reported catalysts for the anodic oxidation of amines[a]

Catalyst	Onset Potential	FE	Ref
Mn-α-$Ni(OH)_2$	1.31	96	This work
NiSe	1.34	99	17
VR-$Ni(OH)_2$[b]	1.36 (10 mA/cm^{-2})	96.5	18
Co-β-$Ni(OH)_2$	1.29	94.89	19

a. Benzyl amines. [b]. Propylamine

References

1. *Nat. Commun*. **2013**, *4*, 2213.
2. *Comput. Mater. Sci.* **1996**, *6*, 15.
3. *Comput. Mater. Sci*. **1996**, *6*, 15.
4. *J. Comput. Chem*. **2006**, *27*, 1787.
5. *Phys. Rev. B: Condens. Matter Mater. Phys.* **1999**, *59*, 1758.
6. *J. Chem. Phys.* **2015**, *142*, 064107.
7. *Computational Materials Science* **2014**, *81*, 446
8. *SoftwareX* **2017**, *6*, 278.
9. *J. Am. Chem. Soc*. **2016**, *138*, 483
10. *Nano Energ*. **2020**, *75*, 104885
11. *J. Electrochem. Soc.* **2006**, *153*, A210.
12. *J. Am. Chem. Soc*. **2018**, *140*, 6745.
13. *PNAS* **2018**, *115*, 5872.
14. *Nanoscale* **2019**, *11*, 16810–16827
15. *ACS Catal*. **2018**, *8*, 5533−5541.
16. *J. Mater. Chem. A* **2021**, *9*, 17521-17527
17. *Angew. Chem. Int. Ed.* **2018**, *57*, 13163.
18. *Angew. Chem. Int. Ed.* **2020**, *59*, 16974.
19. *Chem* **2020**, *6*, 2974.